Available online at www.sciencedirect.com
ScienceDirect
Comput. Methods Appl. Mech. Engrg. 340 (2018) 121–146
Computer methods in applied mechanics and engineering
www.elsevier.com/locate/cma

A modified dual-level fast multipole boundary element method based on the Burton–Miller formulation for large-scale three-dimensional sound field analysis

Junpu Li[a,b], Wen Chen[a,*], Qinghua Qin[b]

[a] *State Key Laboratory of Hydrology-Water Resources and Hydraulic Engineering & Center for Numerical Simulation Software in Engineering and Sciences, College of Mechanics and Materials, Hohai University, Nanjing, Jiangsu, 211100, China*
[b] *College of Engineering and Computer Science, Australian National University, Canberra ACT 2601, Australia*

Received 8 March 2018; received in revised form 9 May 2018; accepted 15 May 2018
Available online 6 June 2018

Highlights

- Excessive storage requirements and ill-conditioning of the BEM are avoided.
- The Burton–Miller formulations are used to overcome the non-uniqueness difficulties.
- The FMM is adopted to expedite the solving process.
- The acoustic scattering characteristics of the Kilo-class submarine are investigated.
- The acoustic scattering characteristics of an A-320 aircraft are investigated.

Abstract

Large-scale sound field analysis is a difficult task for numerical simulations. In this study, a modified dual-level fast multipole boundary element method is proposed for analyzing this challenging problem. The proposed method is based on the Burton–Miller formulation to overcome the non-uniqueness issues in exterior acoustic problems. By transforming the fully-populated matrix formed from fine mesh to a large-scale locally supported sparse matrix induced from coarse mesh, the method overcomes computational bottleneck of the boundary element method originating from excessive storage requirements and the large number of operations. In this article, we further combine the method with the fast multipole method to expedite its matrix vector multiplications process. By testing the method to a series of complicated engineering cases, it is observed that the method performs 44% faster than COMSOL in the analysis of acoustic scattering characteristics of an A-320 aircraft. In the analysis of underwater

* Corresponding author.
E-mail addresses: junpu.li@foxmail.com (J.P. Li), chenwen@hhu.edu.cn (W. Chen).

https://doi.org/10.1016/j.cma.2018.05.016

acoustic scattering characteristics of the Kilo-class submarine, the method is 56% faster than the traditional fast multipole boundary element method.

Keywords: Modified dual-level algorithm; Boundary element method; Fast multipole method; Finite element method; Large-scale sound field analysis

1. Introduction

Sound field analysis plays an important role in practical engineering computation, such as the vibration analysis [1], the underwater sonar imaging detection [2] and the active noise control [3]. It is recognized that large-scale sound field analysis is a difficult and challenging topic in numerical computation, especially for the large-scale high frequency sound field analysis [4–6]. That is because most of the acoustic problems are usually posted on infinite domain [7], and one has to solve the resulting large-scale and highly ill-conditioned linear system of equations [8,9].

The traditional finite element method (FEM) [10–13] has to be artificially truncated to satisfy the radiation conditions at infinity. As a global discretization method, the number of degree of freedoms (DOFs) of the FEM increases by cube of wavenumber, and in fact worse than that due to the pollution effect [14].

The boundary element method (BEM) [15–18] and the boundary collocation methods [19–21], such as the singular boundary method (SBM) [22–25] and the method of fundamental solutions (MFS) [26–29], use the fundamental solutions as their basis function. This type of methods need only boundary discretization and satisfy automatically the radiation conditions at infinity. Therefore, one dimension is reduced for solving problems. Their number of DOFs increases by square of wavenumber. Unfortunately, these methods usually result in a fully-populated matrix, which brings a large number of operations and excessive storage requirements for large-scale problems. To remedy this drawback, a variety of fast algorithms has been proposed in the past decades, such as the fast multipole method (FMM) [30–32], the precorrected-fast Fourier transform method (PFFT) [33] and the multilevel fast multipole algorithm (MLFMA) [34,35]. However, all these methods have their own merits and drawbacks. The FMM is not efficient in evaluating the far-field contributions. The PFFT requires uniform discretization of the whole boundary. The MLFMA is too complicated in terms of programming. In addition, all of these above-mentioned methods need to be combined with the preconditioning techniques [36,37] to reduce iteration number of the iterative solver, such as the generalized minimal residual algorithm (GMRES) [38] solver.

In this study, we propose a modified dual-level fast multipole boundary element method (DL-FMBEM) based on the Burton–Miller formulation for large-scale sound field analysis. The DL-FMBEM is a novel numerical method to solve the computational bottleneck encountered by the traditional BEM in simulation of large-scale problems. The core feature of the DL-FMBEM is that the fully-populated matrix formed from the fine mesh is transformed to a sparse matrix induced from the coarse mesh. The large number of operations and excessive storage requirements originating from the fully-populated and highly ill-conditioned matrix are hereby avoided.

As a well-known powerful fast algorithm, there are two types of FMM. They are the low frequency FMM [39,40] and the high frequency FMM [41,42]. The low frequency FMM relies on the partial wave expansion of the fundamental solutions and has $O(N)$ computation complexity. Its expansion formulations are related to $O(p^5)$, where p is truncation term of the FMM. The required truncation term number increases fast with the increase of wavenumber. Therefore, the low frequency FMM in general are good only for lower frequency acoustic problems. The high frequency FMM relies on the plane wave expansion of the fundamental solutions and has $O(N \log N)$ computation complexity. This diagonal form FMM can be used to expedite the computations of all the translations. Unfortunately, it breaks down at a lower frequency. In this study, we first use the above low frequency FMM to expedite the matrix vector multiplications process of the DL-FMBEM. The total number of operations and storage requirements of the DL-FMBEM are hereby reduced to $O(N)$ from $O(N^2)$.

Prior to this study, the modified dual-level algorithm [43] has already been applied for potential theory. However, Ref. [43] focuses only on establishment of the algorithm for potential theory, and the complicated engineering analysis is missing. This study extends the DL-FMBEM to acoustic theory, and the Burton–Miller formulation [44] is combined with the DL-FMBEM to overcome the non-uniqueness issues for exterior acoustic problems.

In subsequent section, a variety of complicated engineering cases is investigated by using the DL-FMBEM, such as the underwater acoustic scattering characteristics of the Kilo-class submarine and the acoustic scattering characteristics of an A-320 aircraft. In particular, we make a comparison between the DL-FMBEM and the mature commercial software COMSOL to show potential of the DL-FMBEM for large-scale sound field analysis.

The article is organized as follows: Section 2 introduces the methodology of the DL-FMBEM and its conjunction with the Burton–Miller formulation. Section 3 investigates a variety of complicated engineering cases by using the DL-FMBEM based on the Burton–Miller formulation. Section 4 makes some conclusions about the results reported. Section 5 gives an outlook based on the present study.

2. Numerical methodology

This section is organized as follows: Sections 2.1 and 2.2 review respectively the basic formulations of the BEM and the FMBEM based on the Burton–Miller formulation. Section 2.3 presents the methodology of the DL-FMBEM based on the Burton–Miller formulation, which constitutes the main contribution of this study.

2.1. Basic formulations of the boundary element method

The governing equation of the propagation of sound wave in isotropic medium can be reduced to the Helmholtz equation [45]

$$\nabla^2\phi(x) + k^2\phi(x) = 0, \forall x \in \Omega, \tag{1}$$

$$\phi(x) = \overline{\phi}(x), \forall x \in S_1, \tag{2}$$

$$q(x) = \overline{q}(x), \forall x \in S_2, \tag{3}$$

where $\phi(x)$ is the acoustic pressure, $q(x)$ denotes the normal derivative of acoustic pressure. $k = 2\pi f/c$ is the wavenumber, c the sound speed, f the frequency, Ω the computational domain, S the computational boundary and ∇^2 represents the Laplacian operator.

The acoustic pressure $\phi(x)$ is expressed by [46–48]

$$\phi(x) = \int_S \left[G(x,y)q(y) - \frac{\partial G(x,y)}{\partial n(y)}\phi(y) \right] dS(y) + \phi^I(x), \forall x \in \Omega, \tag{4}$$

where $\phi^I(x)$ represents the incident wave, x and y are the source point and field point, respectively. The fundamental solutions of the 3-D Helmholtz equation are

$$\begin{cases} G(x,y) = \dfrac{e^{ikr}}{4\pi r} \\ F(x,y) = \dfrac{\partial G(x,y)}{\partial n(y)} = \dfrac{e^{ikr}}{4\pi r^2}(ikr-1)\left\langle (x,y)\cdot n(y) \right\rangle, \end{cases} \tag{5}$$

where $i = \sqrt{-1}$, $r = |x - y|$ and $n(y)$ is the outward normal at point y.

When $x \to S$, the following conventional boundary integral equation (CBIE) is given

$$C(x)\phi(x) = \int_S \left[G(x,y)q(y) - \frac{\partial G(x,y)}{\partial n(y)}\phi(y) \right] dS(y) + \phi^I(x), \forall x \in S, \tag{6}$$

where $C(x) = \frac{1}{2}$ when the boundary S is smooth.

Similarly, we have the following hypersingular boundary integral equation (HBIE)

$$C(x)q(x) = \int_S \left[\frac{\partial G(x,y)}{\partial n(x)}q(y) - \frac{\partial^2 G(x,y)}{\partial n(y)\partial n(x)}\phi(y) \right] dS(y) + q^I(x), \forall x \in S, \tag{7}$$

where $C(x) = \frac{1}{2}$ when the boundary S is smooth, and

$$\begin{cases} K(x,y) = \dfrac{\partial G(x,y)}{\partial n(x)} = -\dfrac{e^{ikr}}{4\pi r^2}(ikr-1)\left\langle (x,y)\cdot n(x) \right\rangle \\ H(x,y) = \dfrac{\partial^2 G(x,y)}{\partial n(y)\partial n(x)} = \dfrac{e^{ikr}}{4\pi r^3}\left[\begin{array}{l} (1-ikr)\left\langle n(y)\cdot n(x) \right\rangle \\ +(k^2r^2-3+3kri)\left\langle (x,y)\cdot n(y) \right\rangle \left\langle (x,y)\cdot n(x) \right\rangle \end{array} \right]. \end{cases} \tag{8}$$

One combines Eq. (6) with Eq. (7) (CHBIE) to overcome the non-uniqueness difficulties for exterior acoustic problems, which is also referred to as the Burton–Miller formulation [44].

$$\begin{aligned}&\left[\int_S \frac{\partial G(x,y)}{\partial n(y)}\phi(y)dS(y) + C(x)\phi(x) - \phi^I(x)\right] + \alpha\int_S \frac{\partial^2 G(x,y)}{\partial n(y)\partial n(x)}\phi(y)dS(y)\\ &= \int_S G(x,y)q(y)dS(y) + \alpha\left[\int_S \frac{\partial G(x,y)}{\partial n(x)}q(y)dS(y) - C(x)q(x) + q^I(x)\right], \forall x \in S,\end{aligned} \tag{9}$$

where $\alpha = i/k$ [49] is the coupling constant.

The discretized form of CHBIE is given by Eq. (10). It is noted that the constant element and boundary collocation method are adopted in this study,

$$\sum_{j=1}^{N} f_{ij}\phi_j = \sum_{j=1}^{N} g_{ij}q_j + \hat{b}_i, \tag{10}$$

where $\hat{b}_i$ is the value of the incident wave at the ith node, and

$$f_{ij}\phi_j = \int_{\Delta S_j} \frac{\partial G(x,y)}{\partial n(y)}\phi_j dS(y) + \frac{1}{2}\delta_{ij}\phi_j + \alpha\int_{\Delta S_j} \frac{\partial^2 G(x,y)}{\partial n(y)\partial n(x)}\phi_j dS(y), \tag{11}$$

$$g_{ij}q_j = \int_{\Delta S_j} G(x,y)q_j dS(y) + \alpha\left[\int_{\Delta S_j} \frac{\partial G(x,y)}{\partial n(x)}q_j dS(y) - \frac{1}{2}\delta_{ij}q_j\right]. \tag{12}$$

By moving the unknown terms to left-hand side and moving the known terms to right-hand side. Eq. (10) is reformulated as

$$A\lambda = b, \tag{13}$$

where A is the interpolation matrix, λ the unknown terms and b the known right-hand side terms. The subtraction and adding-back technique (see, e.g., [43,50–52]) is used to evaluate the singular and hypersingular terms in Eq. (13). The details of the technique are given in Appendix.

2.2. Basic formulations of the fast multipole boundary element method based on the Burton–Miller formulation

The basic formulations of the FMBEM based on the Burton–Miller formulation are reviewed in this section. Most of the expansions and translations can be found in Refs. [53–55].

The multipole expansion of the fundamental solution $G(x, y)$ is written as

$$G(x,y) = \frac{ik}{4\pi}\sum_{n=0}^{\infty}(2n+1)\sum_{m=-n}^{n}\overline{I}_n^m(k, y-y_c)O_n^m(k, x-y_c),\ |y-y_c| < |x-y_c|, \tag{14}$$

where y_c is the expansion center, the inner function I_n^m is defined by

$$I_n^m(k, y-y_c) = j_n(k|y-y_c|)Y_n^m\left(\frac{y-y_c}{|y-y_c|}\right), \tag{15}$$

$\overline{I}_n^m$ is the complex conjugate of I_n^m, and the outer function is

$$O_n^m(k, x-y_c) = h_n^{(1)}(k|x-y_c|)Y_n^m\left(\frac{x-y_c}{|x-y_c|}\right), \tag{16}$$

where j_n is the nth order spherical Bessel function of the first kind, $h_n^{(1)}$ the nth order spherical Hankel function of the first kind, and Y_n^m the spherical harmonics,

$$Y_n^m(x) = \sqrt{\frac{(n-m)!}{(n+m)!}}P_n^m(\cos\theta)e^{im\varphi},\ \text{for } n = 1, 2, 3\ldots, m = -n, \ldots, n, \tag{17}$$

where (ρ, θ, φ) is the coordinates of x. P_n^m denotes the associated Legendre function,

$$P_n^m(x) = (1-x^2)^{m/2}\frac{d^m}{dx^m}P_n(x), \tag{18}$$

where $P_n(x)$ represents the Legendre polynomials of degree n.

Similarly, the fundamental solution $F(x, y)$ is expanded as

$$F(x,y) = \frac{ik}{4\pi}\sum_{n=0}^{\infty}(2n+1)\sum_{m=-n}^{n} O_n^m(k, x-y_c)\frac{\partial \overline{I}_n^m(k, y-y_c)}{\partial n(y)}, |y-y_c| < |x-y_c|. \tag{19}$$

Based on above multipole expansion formulations, the following formulations are given

$$\int_{S_c} G(x,y)q(y)dS(y) = \frac{ik}{4\pi}\sum_{n=0}^{\infty}(2n+1)\sum_{m=-n}^{n} M_{n,m}(k, y_c)O_n^m(k, x-y_c), |y-y_c| < |x-y_c|, \tag{20}$$

$$\int_{S_c} F(x,y)\phi(y)dS(y) = \frac{ik}{4\pi}\sum_{n=0}^{\infty}(2n+1)\sum_{m=-n}^{n} \widetilde{M}_{n,m}(k, y_c)O_n^m(k, x-y_c), |y-y_c| < |x-y_c|, \tag{21}$$

where $M_{n,m}$ and $\widetilde{M}_{n,m}$ are called as the multipole moments with center y_c,

$$M_{n,m}(k, y_c) = \int_{S_c} \overline{I}_n^m(k, y-y_c)q(y)dS(y), \tag{22}$$

$$\widetilde{M}_{n,m}(k, y_c) = \int_{S_c} \frac{\partial \overline{I}_n^m(k, y-y_c)}{\partial n(y)}\phi(y)dS(y). \tag{23}$$

Then, the following M2M translation is introduced to move the multipole moment center from y_c to $y_{c'}$

$$M_n^m(k, y_{c'}) = \sum_{n'=0}^{\infty}\sum_{m'=-n'}^{n'}\sum_{\substack{l=|n-n'|\\ n+n'-l:even}}^{n+n'} (2n'+1)(-1)^{m'}W_{n,n',m,m',l}\times I_l^{-m-m'}(k, y_c-y_{c'})M_{n',-m'}(k, y_c), \tag{24}$$

where $|y-y_{c'}| < |x-y_{c'}|$ and

$$W_{n,n',m,m',l} = (2l+1)i^{n'-n+l}\begin{pmatrix} n & n' & l \\ 0 & 0 & 0\end{pmatrix}\times\begin{pmatrix} n & n' & l \\ m & m' & -m-m'\end{pmatrix}, \tag{25}$$

where $\begin{pmatrix} * & * & * \\ * & * & *\end{pmatrix}$ is the Wigner $3j$ symbol [56].

The local expansion of $G(x, y)$ in CBIE is written as

$$\int_{S_c} G(x,y)q(y)dS(y) = \frac{ik}{4\pi}\sum_{n=0}^{\infty}(2n+1)\sum_{m=-n}^{n} L_{n,m}(k, x_L)\overline{I}_n^m(k, x-x_L). \tag{26}$$

The local expansion coefficients of Eq. (26) can be evaluated by using the M2L translation

$$L_{n,m}(k, x_L) = \sum_{n'=0}^{\infty}(2n'+1)\sum_{m'=-n'}^{n'}\sum_{\substack{l=|n-n'|\\ n+n'-l:even}}^{n+n'} W_{n',n,m',m,l}\widetilde{O}_l^{-m-m'}(k, x_L-y_c)\times M_{n',m'}(k, y_c), \tag{27}$$

where $|x-x_L| < |y_c-x_L|$, x_L is the center of the local expansion, and $\widetilde{O}_n^m$ is given by

$$\widetilde{O}_n^m(k, x) = h_n^{(1)}(k|x|)\overline{Y}_n^m\left(\frac{x}{|x|}\right). \tag{28}$$

Similarly, the local expansion of $F(x, y)$ in CBIE is written as

$$\int_{S_c} F(x,y)\phi(y)dS(y) = \frac{ik}{4\pi}\sum_{n=0}^{\infty}(2n+1)\sum_{m=-n}^{n} L_{n,m}(k, x_L)\overline{I}_n^m(k, x-x_L), \tag{29}$$

and the local expansion coefficients of Eq. (29) is

$$L_{n,m}(k,x_L)=\sum_{n'=0}^{\infty}(2n'+1)\sum_{m'=-n'}^{n'}\sum_{\substack{l=|n-n'|\\ n+n'-l:even}}^{n+n'} W_{n',n,m',m,l}\widetilde{O}_l^{-m-m'}(k,x_L-y_c)\times\widetilde{M}_{n',m'}(k,y_c). \tag{30}$$

For the HBIE, the local expansion of $K(x,y)$ is defined as

$$\int_{S_c}K(x,y)q(y)dS(y)=\frac{ik}{4\pi}\sum_{n=0}^{\infty}(2n+1)\sum_{m=-n}^{n}L_{n,m}(k,x_L)\frac{\partial\overline{I}_n^m(k,x-x_L)}{\partial n(x)}, \tag{31}$$

and the local expansion coefficients of Eq. (31) is

$$L_{n,m}(k,x_L)=\sum_{n'=0}^{\infty}(2n'+1)\sum_{m'=-n'}^{n'}\sum_{\substack{l=|n-n'|\\ n+n'-l:even}}^{n+n'} W_{n',n,m',m,l}\widetilde{O}_l^{-m-m'}(k,x_L-y_c)\times M_{n',m'}(k,y_c). \tag{32}$$

The local expansion of $H(x,y)$ is defined as

$$\int_{S_c}H(x,y)\phi(y)dS(y)=\frac{ik}{4\pi}\sum_{n=0}^{\infty}(2n+1)\sum_{m=-n}^{n}L_{n,m}(k,x_L)\frac{\partial\overline{I}_n^m(k,x-x_L)}{\partial n(x)}, \tag{33}$$

and the local expansion coefficients of Eq. (33) is

$$L_{n,m}(k,x_L)=\sum_{n'=0}^{\infty}(2n'+1)\sum_{m'=-n'}^{n'}\sum_{\substack{l=|n-n'|\\ n+n'-l:even}}^{n+n'} W_{n',n,m',m,l}\widetilde{O}_l^{-m-m'}(k,x_L-y_c)\times\widetilde{M}_{n',m'}(k,y_c). \tag{34}$$

The following L2L translation is given to move the local expansion center from L to L',

$$L_{n,m}(k,x_{L'})=\sum_{n'=0}^{\infty}\sum_{m'=-n'}^{n'}\sum_{\substack{l=|n-n'|\\ n+n'-l:even}}^{n+n'}(2n'+1)(-1)^m W_{n',n,m',-m,l}\times I_l^{m-m'}(k,x_{L'}-x_L)L_{n',m'}(k,x_L). \tag{35}$$

Finally, the far-field contributions for the Dirichlet boundary conditions are evaluated by using the following local expansion

$$f_{ij}\phi_j=\frac{ik}{4\pi}\sum_{n=0}^{\infty}(2n+1)\sum_{m=-n}^{n}L_{n,m}(k,x_L)\times\left[\overline{I}_n^m(k,x_i-x_L)+\alpha\frac{\partial\overline{I}_n^m(k,x_i-x_L)}{\partial n(x_i)}\right]. \tag{36}$$

The far-field contributions for the Neumann boundary conditions are evaluated by

$$g_{ij}q_j=\frac{ik}{4\pi}\sum_{n=0}^{\infty}(2n+1)\sum_{m=-n}^{n}L_{n,m}(k,x_L)\times\left[\overline{I}_n^m(k,x_i-x_L)+\alpha\frac{\partial\overline{I}_n^m(k,x_i-x_L)}{\partial n(x_i)}\right]. \tag{37}$$

2.3. The modified dual-level fast multipole boundary element method based on the Burton–Miller formulation

In this section, the modified dual-level algorithm and its conjunction with the FMBEM based on the Burton–Miller formulation are presented. The core idea of the DL-FMBEM is to transform the fully-populated matrix on fine mesh to a locally supported sparse matrix by neglecting the residuals of the far-field contributions [43]. In the DL-FMBEM, although the interpolation matrix on coarse mesh is still fully-populated, it is smaller in scale and its evaluation can be expedited by the FMM. By the help of the dual-level structure, on one hand, the far-field interactions are assessed only by coarse mesh. On the other hand, the resulting locally supported sparse matrix on fine mesh can be effectively solved by using the iterative solver due to its sparsity.

In subsequent section, we present the logical process of the DL-FMBEM based on the Burton–Miller formulation to solve the linear system of equations given in Eq. (13). The following nomenclatures are listed in Table 1 for clear and concise deduction process.

Table 1
Nomenclature in the DL-FMBEM based on the Burton–Miller formulation.

$\lambda^0_{\Omega_1}$	Initial approximate solution on coarse mesh	A	Interpolation matrix
$\lambda^0_{\Omega_2}$	Initial approximate solution on fine mesh	b	The known right-hand side terms
$\alpha^0_{\Omega_2}$	Initial residual potential solution on fine mesh	C_{Ω_2}	Sparse matrix on fine mesh
$\gamma^0_{\Omega_2}$	Initial accurate solution on fine mesh	Ω_1	Coarse mesh subscript
$V^0_{\Omega_2}$	Initial approximate residual potential on fine mesh	Ω_2	Fine mesh subscript
$\alpha^k_{\Omega_1}$	The kth residual potential solution on coarse mesh	I^+	Positive projection operator
$\chi^k_{\Omega_2}$	The kth accurate residual potential on fine mesh	I^-	Negative projection operator
$\chi^k_{\Omega_1}$	The kth accurate residual potential on coarse mesh	N_{Ω_2}	Number of fine-mesh elements
$\alpha^{k+1}_{\Omega_2}$	The $(k+1)$th residual potential solution on fine mesh	N_{Ω_1}	Number of coarse-mesh elements
$\lambda^{k+1}_{\Omega_2}$	The $(k+1)$th approximate solution on fine mesh	Tol	Preset convergence criterion
$Rerr^0_{\Omega_2}$	Initial average relative error on fine mesh	x^i	The ith source point
$Rerr^{k+1}_{\Omega_2}$	The $(k+1)$th average relative error on fine mesh	y^i	The ith field point
$\gamma^{k+1}_{\Omega_2}$	The $(k+1)$th accurate solution on fine mesh		
$V^{k+1}_{\Omega_2}$	The $(k+1)$th approximate residual potential on fine mesh		
r_0	Characteristic radius of range of influence of near field region		

In this article, the average value of the coarse-mesh element is used as the values of its corresponding fine-mesh elements, i.e., $Value_2 = Value_1/Sep$, where we suppose that every coarse-mesh element is divided into Sep fine-mesh elements. That is $I^+ : \Omega_1 \to \Omega_2$, which represents the positive projection operator. The sum of values of the fine-mesh elements is used as value of their corresponding coarse-mesh element, i.e., $Value_1 = \sum_{i=1}^{Sep} Value_2^i$. That is $I^- = \Omega_2 \to \Omega_1$, which is the negative projection operator.

***Step* 1** Evaluating the $\lambda^0_{\Omega_2}$ (Coarse mesh).

***Substep* 1.1** Solving the linear system of equations on coarse mesh

$$A_{\Omega_1}\lambda^0_{\Omega_1} = b_{\Omega_1}, \tag{38}$$

***Substep* 1.2** Mapping the $\lambda^0_{\Omega_1}$ onto the fine mesh

$$\lambda^0_{\Omega_2} = I^+\lambda^0_{\Omega_1}, \tag{39}$$

***Step* 2** Evaluating the $\gamma^0_{\Omega_2}$ (Fine mesh).

***Substep* 2.1** Evaluating the $V^0_{\Omega_2}$,

$$V^0_{\Omega_2} = b_{\Omega_2} - A_{\Omega_2}\lambda^0_{\Omega_2}. \tag{40}$$

***Substep* 2.2** Evaluating the $\alpha^0_{\Omega_2}$,

$$C_{\Omega_2}\alpha^0_{\Omega_2} = V^0_{\Omega_2}, \tag{41}$$

where C_{Ω_2} satisfies the following condition:

if $\left|x^i_{\Omega_2} - y^j_{\Omega_2}\right| > r_0$
  $C^{ij}_{\Omega_2} = 0$;
else if $\left|x^i_{\Omega_2} - y^j_{\Omega_2}\right| \le r_0$
  $C^{ij}_{\Omega_2} = A^{ij}_{\Omega_2}$;
end

***Substep* 2.3** Evaluating the $\gamma^0_{\Omega_2}$,

$$\gamma^0_{\Omega_2} = \alpha^0_{\Omega_2} + \lambda^0_{\Omega_2}. \tag{42}$$

Step 3 Assessing the $Rerr^0_{\Omega_2}$ (Fine mesh),

$$Rerr^0_{\Omega_2} = \sqrt{\sum_{i=1}^{N_{\Omega_2}} \left| b^i_{\Omega_2} - \sum_{j=1}^{N_{\Omega_2}} A^{ij}_{\Omega_2} \left(\gamma^0_{\Omega_2}\right)_j \right|^2 \Big/ \sum_{i=1}^{N_{\Omega_2}} \left| b^i_{\Omega_2} \right|^2}. \tag{43}$$

The condition of the recursive computation satisfies:

if $Rerr^0_{\Omega_2} > Tol$
    enter *Step* 4;
else if $Rerr^0_{\Omega_2} \leq Tol$
    program ends;
end

... Assuming the $\gamma^k_{\Omega_2}$ is obtained after k times loops.

Step 4 Evaluating the $\chi^k_{\Omega_1}$ (Fine mesh).

Substep 4.1 Evaluating the $\chi^k_{\Omega_2}$,

$$\chi^k_{\Omega_2} = b_{\Omega_2} - A_{\Omega_2}\gamma^k_{\Omega_2}. \tag{44}$$

Substep 4.2 Evaluating the $\chi^k_{\Omega_1}$,

$$\chi^k_{\Omega_1} = I^- \chi^k_{\Omega_2}. \tag{45}$$

Step 5 Evaluating the $\alpha^k_{\Omega_1}$(Coarse mesh),

$$A_{\Omega_1}\alpha^k_{\Omega_1} = \chi^k_{\Omega_1}. \tag{46}$$

Step 6 Evaluating the $\gamma^{k+1}_{\Omega_2}$ (Fine mesh),

Substep 6.1 Evaluating the $\lambda^{k+1}_{\Omega_2}$,

$$\lambda^{k+1}_{\Omega_2} = \gamma^k_{\Omega_2} + I^+\alpha^k_{\Omega_1}. \tag{47}$$

Substep 6.2 Evaluating the $V^{k+1}_{\Omega_2}$,

$$V^{k+1}_{\Omega_2} = b_{\Omega_2} - A_{\Omega_2}\lambda^{k+1}_{\Omega_2}. \tag{48}$$

Substep 6.3 Evaluating the $\alpha^{k+1}_{\Omega_2}$,

$$C_{\Omega_2}\alpha^{k+1}_{\Omega_2} = V^{k+1}_{\Omega_2}, \tag{49}$$

Substep 6.4 Evaluating the $\gamma^{k+1}_{\Omega_2}$,

$$\gamma^{k+1}_{\Omega_2} = \alpha^{k+1}_{\Omega_2} + \lambda^{k+1}_{\Omega_2}. \tag{50}$$

Step 7 Assessing the $Rerr^{k+1}_{\Omega_2}$ (Fine mesh),

$$Rerr^{k+1}_{\Omega_2} = \sqrt{\sum_{i=1}^{N_{\Omega_2}} \left| b^i_{\Omega_2} - \sum_{j=1}^{N_{\Omega_2}} A^{ij}_{\Omega_2} \left(\gamma^{k+1}_{\Omega_2}\right)_j \right|^2 \Big/ \sum_{i=1}^{N_{\Omega_2}} \left| b^i_{\Omega_2} \right|^2}. \tag{51}$$

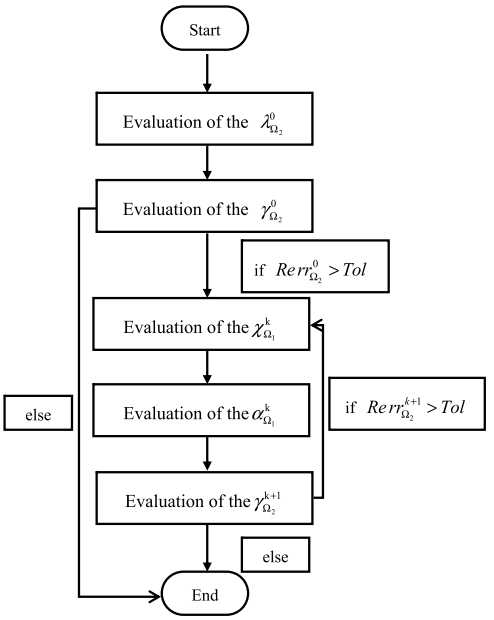

Fig. 1. Block diagram of the DL-FMBEM based on the Burton–Miller formulation.

The condition of ending of the program satisfies:

if $Rerr^{k+1}_{\Omega_2} \leq Tol$
    program ends;
else if $Rerr^{k+1}_{\Omega_2} > Tol$
    enter *Step* 4;
end

It is noted that the calculation of Eqs. (38), (40), (43), (44), (46), (48) and (51) are expedited via the FMM. The block diagram is plotted in Fig. 1.

3. Numerical results and discussions

In this study, we use two indexes to assess the numerical characteristics of the DL-FMBEM. They are the average relative errors (*Error*) and the average relative error on boundary (*Rerr*). The index *Error* is to investigate the overall convergence of numerical methods, and the index *Rerr* is to assess solution quality of the linear system of equations.

$$Error = \sqrt{\sum_{i=1}^{NT} |u(i) - \overline{u}(i)|^2 \Big/ \sum_{i=1}^{NT} |\overline{u}\,(i)|^2}, \tag{52}$$

$$Rerr = \sqrt{\sum_{i=1}^{N} \left| b_i - \sum_{j=1}^{N} A_{ij}\lambda_j \right|^2 \Big/ \sum_{i=1}^{N} |b_i|^2}, \tag{53}$$

where $\overline{u}\,(i)$ and $u\,(i)$ are the analytical and numerical solution at point x_i, respectively. NT is the number of test points and N represents the number of DOFs.

The convergence rate C is assessed by

$$C = -2\frac{\ln\left(Error\,(N_1)\right) - \ln\left(Error\,(N_2)\right)}{\ln\left(N_1\right) - \ln\left(N_2\right)}, \tag{54}$$

where $Error\,(N_1)$ and $Error\,(N_2)$ are the errors of numerical solutions with DOFs of N_1 and N_2.

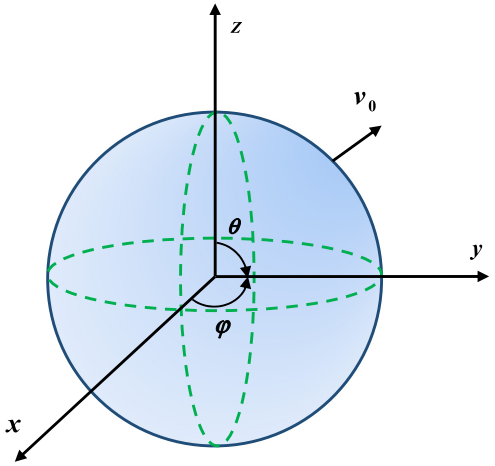

Fig. 2. The pulsating sphere model.

All subsequent results are computed on a single laptop with an Intel Core i7-4710MQ 2.50 GHz Processor and 16 GB RAM. The Matlab 2016b and COMSOL Multiphysics 5.3a are used to obtain the following results. In the FMM, the precision flag ε is defined as $p = -\log_2(\varepsilon)$ [32], where p is the truncation term number. If there is no particular emphasis, the precision flag of the FMM, the DL-FMBEM and the GMRES solver are set as 5e−4, 1e−4 and 1e−4, respectively. And we take $r_0 = 3R^0_{\Omega_1}$ in the study, where $R^0_{\Omega_1}$ represents the average characteristic radius of coarse-mesh element.

Example 1a (*Dirichlet Boundary Conditions*)**.** The pulsating sphere model is a benchmark example to test numerical methods. In the model, every point on the sphere vibrates with the same amplitude, phase and velocity as shown in Fig. 2. This model is governed by the 3-D Helmholtz equation. The resulting sound field is called the pulsating sphere radiated sound field. The analytical solution is [57],

$$\phi(r) = v_0 \frac{ikc\rho a^2}{(1-ika)} \frac{e^{ik(r-a)}}{r}$$

where $a = 1$ m is radius of the pulsating sphere, $c = 343$ m/s the sound velocity, $\rho = 1.2$ kg/m^3 the air density, $v_0 = 3$ m/s the velocity of vibration, and k represents the wavenumber. The test points are placed on a sphere surface with radius 3 m.

Case 1 Numerical convergence of the DL-FMBEM is investigated in this case. The number of coarse-mesh elements is taken as 1600, wavenumber k is set as 10. We plot Fig. 3 to show convergence of the DL-FMBEM against number of DOFs.

It is observed from Fig. 3 that the DL-FMBEM based on the Burton–Miller formulation converges remarkably with order of 2.8, which is similar with the convergence rate of the DL-FMBEM without the Burton–Miller formulation. It indicates that the Burton–Miller formulation does not affect accuracy of the DL-FMBEM. Because the number of operations in the DL-FMBEM based on the Burton–Miller formulation is about twice of those of the DL-FMBEM without the Burton–Miller formulation, when the number of DOFs is the same, the computation speed of the DL-FMBEM based on the Burton–Miller formulation is, however, slightly slower than that of the DL-FMBEM without the Burton–Miller formulation.

When number of fine-mesh elements is taken as 101 875, numerical results show that the DL-FMBEM based on the Burton–Miller formulation consumes 434.48 s to obtain the results with *Error* = 2.69e−5. The DL-FMBEM without the Burton–Miller formulation consumes 221.69 s to obtain the similar results. In stark contrast, the FMBEM based

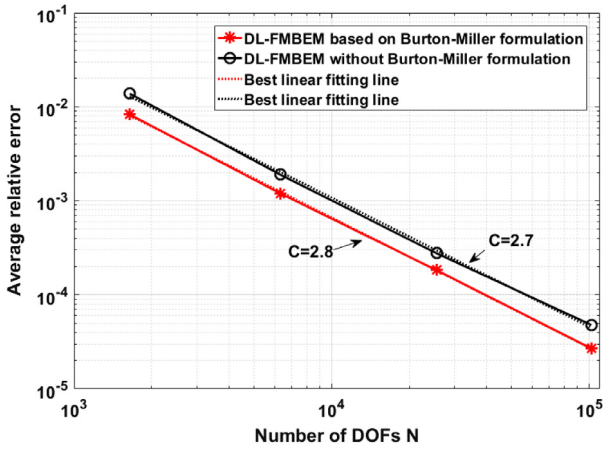

Fig. 3. Convergence of the DL-FMBEM against number of fine-mesh elements.

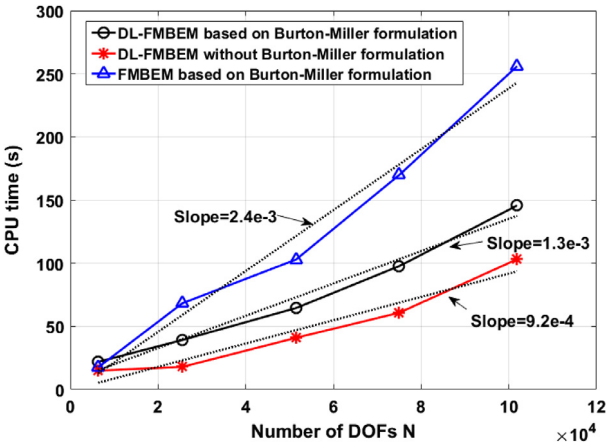

Fig. 4. CPU time of the DL-FMBEM and the FMBEM against number of DOFs.

on the Burton–Miller formulation consumes 1.03e+3 s to obtain the similar results with $Error = 2.52e{-}05$ when the same number of DOFs is taken.

Case 2 Operation efficiency of the proposed method is investigated in this case. The number of coarse-mesh elements is taken as 1600, wavenumber k is 5. We plot Fig. 4 to show the different CPU time of the DL-FMBEM and the FMBEM against number of DOFs.

It is observed from Fig. 4 that the CPU time of the DL-FMBEM and the FMBEM both increase almost linearly along with an increase in the number of DOFs. In addition, it is noted that the slope of CPU time curve of the FMBEM based on the Burton–Miller formulation is about twice of that of the DL-FMBEM based on the Burton–Miller formulation.

Case 3 Storage requirements of the proposed method are investigated in this case. The wavenumber k is taken 1 for simplicity. Results of the DL-FMBEM based on the Burton–Miller formulation are listed in Table 2. We plot Fig. 5 to show the different storage requirements between the sparse matrix on fine mesh of the DL-FMBEM and the fully-populated matrix of the BEM.

It is noted from Fig. 5 that storage requirements of the DL-FMBEM based on the Burton–Miller formulation increases linearly with the number of DOFs increasing. In addition, it is also found from Figs. 4 and 5 that the FMM

Table 2
Results of the DL-FMBEM based on the Burton–Miller formulation.

Coarse-mesh element	1646	6316	13 820	19 000	25 529
Fine-mesh element	6136	25 529	51 480	74 982	101 875
Rerr (*Tol* = 1e−4)	8.71e−6	8.63e−5	7.73e−5	6.30e−5	4.54e−5
Error	2.25e−5	8.88e−5	7.68e−5	6.17e−5	4.42e−5
Ratio of the nonzero elements in C_{Ω_2}	5.72e−3	1.47e−3	6.97e−4	4.95e−4	3.65e−4

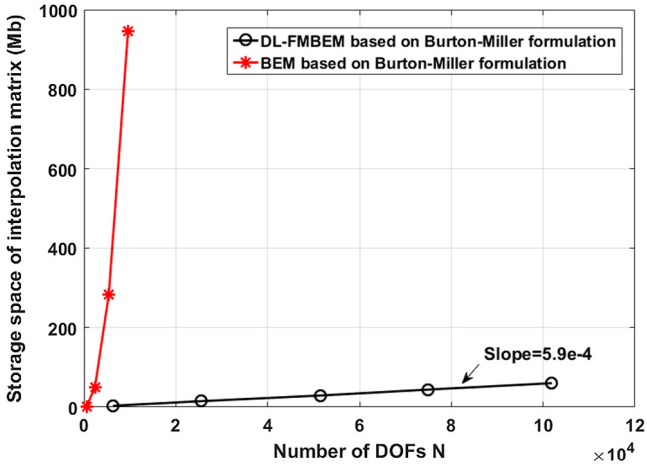

Fig. 5. Storage space of the interpolation matrix of the DL-FMBEM and the BEM.

and the modified dual-level algorithm improve the operation efficiency and reduce the storage requirements of the BEM both to $O(N)$.

Example 1b (*Neumann Boundary Condition*)**.** We take the same pulsating sphere model as in Example 1a. The test points are placed on a sphere surface at radius 3 m. The Neumann boundary conditions are considered, and we evaluate the acoustic pressure around the pulsating sphere. The governing equation is given by

$$\begin{cases} \nabla^2\phi(x,y,z) + k^2\phi = 0, (x,y,z) \in \Omega^e \\ \overline{q}(x,y,z) = \dfrac{\partial\overline{\phi}(x,y,z)}{\partial n}, (x,y,z) \in S \\ \lim\limits_{r\to\infty} r(\dfrac{\partial\phi}{\partial r} - ik\phi) = 0, r = \sqrt{x^2+y^2+z^2}, \end{cases}$$

where

$$\phi(r) = v_0 \frac{ikc\rho a^2}{(1-ika)} \frac{e^{ik(r-a)}}{r}.$$

Case 1 Convergence of the DL-FMBEM with Neumann boundary conditions is investigated here. The number of coarse-mesh elements is taken as 15 284, wavenumber k is taken to be 1, 5 and 10, respectively. We plot Fig. 6 to show the convergence rate of the DL-FMBEM against number of fine-mesh elements.

It is observed from Fig. 6 that convergence of the DL-FMBEM is not affected by the Burton–Miller formulation, different wavenumbers or the Neumann boundary conditions. All convergence curves in Fig. 6 converge remarkably with the increasing number of DOFs.

Case 2 The minimal required sampling frequency on coarse mesh is investigated. The number of fine-mesh elements is taken as 15 284, the wavenumber is taken as 10. Tables 3 and 4 show respectively the numerical results of the DL-FMBEM and the FMBEM against sampling frequencies.

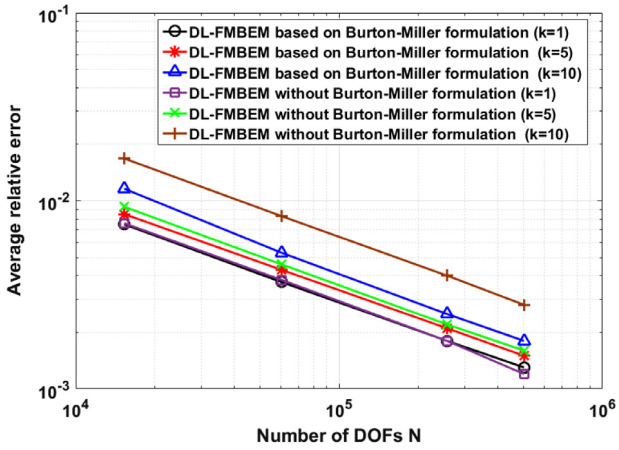

Fig. 6. Average relative error of the DL-FMBEM against fine-mesh elements.

Table 3
Numerical results of the DL-FMBEM against sampling frequencies.

Coarse-mesh element	206	296	402	512	830	1226	2594
Coarse-mesh element /Wavelength (N/λ)	2.54	3.05	3.55	4.01	5.11	6.21	9.03
Rerr ($Tol = 1e{-}4$)	9.08e−5	5.79e−5	5.68e−5	7.43e−5	2.82e−5	4.30e−5	5.22e−5
Error	1.67e−2	1.67e−2	1.66e−2	1.67e−2	1.66e−2	1.66e−2	1.67e−2
CPU time (s)	60.15	17.66	11.06	7.62	7.60	8.65	13.27
Iteration number of *Step* 4–7	34	11	7	5	4	3	2
Ratio of the nonzero elements in C_{Ω_2}	4.30e−2	3.00e−2	2.23e−2	1.74e−2	1.08e−2	7.28e−3	3.41e−3

Table 4
Numerical results of the FMBEM against sampling frequencies.

Boundary element	206	512	830	1226	2594	15 284
Boundary element/Wavelength (N/λ)	2.54	4.01	5.11	6.21	9.03	21.91
Error	2.47e−1	1.14e−1	8.33e−2	6.32e−2	4.23e−2	1.68e−2
CPU time (s)	0.18	0.18	0.50	1.15	2.02	9.77

It is noted that even we take $N/\lambda = 2.54$ on coarse mesh, the DL-FMBEM still can obtain the acceptable solution. It should be mentioned that placing 2.5 DOFs in each wavelength per direction is the minimal requirement allowed by the sampling theorem to obtain a correct solution. In stark contrast, it is noted that one must place almost 22 DOFs in each wavelength per direction in the FMBEM to obtain the acceptable solution.

One can also obtain the following conclusions from Table 3:

(1) The number of coarse-mesh elements does not affect the final accuracy of the DL-FMBEM.

(2) The larger of the sampling frequency on coarse mesh is, the less iteration number of *Step* 4–7 in the DL-FMBEM will be required.

(3) When the number of fine-mesh element is fixed, the consuming CPU time of the DL-FMBEM decreases first and then increases with number of coarse-mesh elements increasing.

Case 3 The non-uniqueness problem of the 3-D exterior acoustic problems is investigated. The boundary condition is given by

$$\overline{q}(x, y, z) = \frac{\partial \overline{\phi}(x, y, z)}{\partial n} \cdot (1 + \delta), (x, y, z) \in S,$$

where δ represents the random noise on boundary. We consider the case with changing frequencies, i.e., frequency sweep, for wavenumber varying from 0.1 to 10. The number of coarse-mesh elements is taken as 943, the number

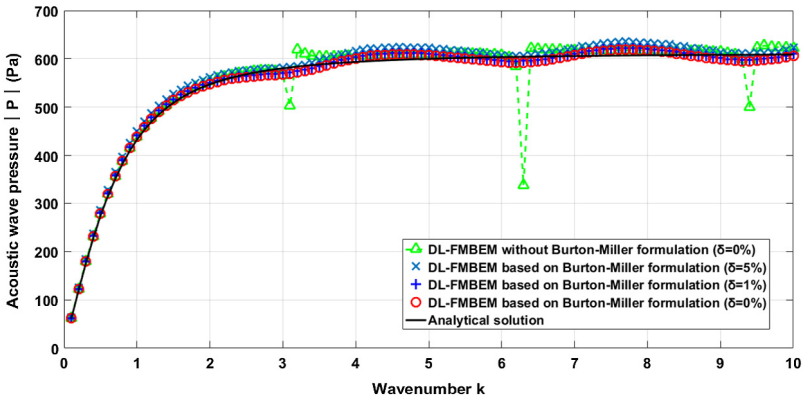

Fig. 7. Frequency-sweep plot of the acoustic pressure $|P|$ (Pa).

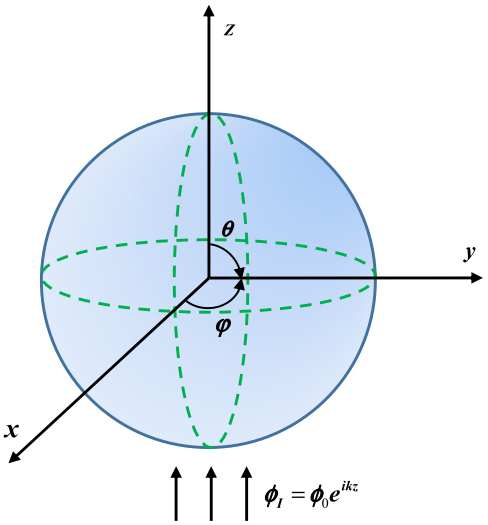

Fig. 8. Scattering of a plane acoustic wave by a unit sphere.

of fine-mesh elements is taken as 3686, and the test point is placed at $(2a, 0, 0)$, The frequency sweep of acoustic pressure is plotted in Fig. 7.

It is observed that the DL-FMBEM based on the Burton–Miller formulation overcomes the non-uniqueness problem near the characteristic frequency. But solution of the DL-FMBEM without the Burton–Miller formulation is in dramatic error at the characteristic frequency. It should be mentioned that computationally troublesome of the singular and hypersingular integrations of the fundamental solutions are both avoided by using the subtraction and adding-back technique. In addition, this technique can be easily expedited via the FMM.

Example 2. Consider the scattering of a plane acoustic wave passing by a sphere obstacle with radius $a = 1$ m as shown in Fig. 8. The sound speed c is 343 m/s, and the test point is placed at $(2a, 0, 0)$. We take 943 coarse-mesh elements and 3686 fine-mesh elements.

The governing equation of this model is also the 3-D Helmholtz equation. An incident plane wave with amplitude $\phi_0 = 1$ traveling in $+Z$ direction is given by

$$\phi_I = \phi_0 e^{ikz}.$$

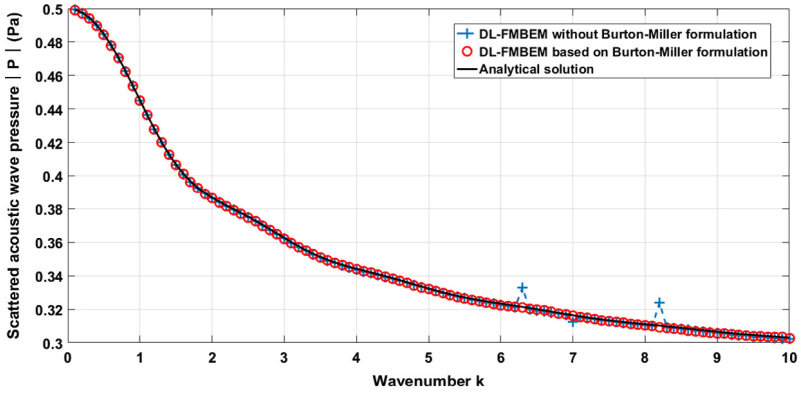

Fig. 9. Frequency-sweep plot of the scattered acoustic pressure $|P|$ (Pa) for soft sphere.

The scattered sound wave is expressed as

$$\phi_S = \sum_{l=0}^{N} \chi_l h_l(kr) P_l(\cos(\theta)),$$

where h_l is the spherical Hankel function of the first kind of order l, P_l the Legendre function of order l, and χ_l the coefficient determined for different boundary conditions.

For soft boundary conditions, the total acoustic pressure on the boundary is zero. That is,

$$\phi_I + \phi_S = 0, \quad at \quad (x, y, z) \in S.$$

The coefficient χ_l for soft boundary conditions is

$$\chi_l = -u_0(2l+1)i^l \frac{j_l(ka)}{h_l(ka)}, \quad a = 1,$$

where j_l is the spherical Bessel function. The scattered sound pressure with the soft boundary conditions against wavenumber is plotted in Fig. 9.

For rigid boundary conditions, the total normal velocity on the boundary is zero, that is,

$$\frac{\partial \phi_s}{\partial n} + \frac{\partial \phi_I}{\partial n} = 0, \quad at \quad r = a.$$

The coefficient χ_l for rigid boundary conditions is

$$\chi_l = -\phi_0(2l+1)i^l \frac{l j_{l-1}(ka) - (l+1) j_{l+1}(ka)}{l h_{l-1}(ka) - (l+1) h_{l+1}(ka)}.$$

The scattered sound pressure with the rigid boundary conditions against wavenumber is plotted in Fig. 10.

It is observed that solution of the DL-FMBEM based on the Burton–Miller formulation is in good agreement with the analytical solution. It is demonstrated that the method can simulate effectively the acoustic scattering problems.

Example 3. Consider the scattering of a plane acoustic wave by a torus-shape obstacle as shown in Fig. 11. The surface of the torus-shape model is defined by

$$\{(x, y, z) \,|x = (R + r\cos\varphi)\cos\theta, y = (R + r\cos\varphi)\sin\theta, z = r\sin\varphi, 0 \le \theta, \varphi < 2\pi\},$$

where $R = 10$ m and $r = 2$ m. The sound speed in water is assumed to be $c = 1480$ m/s. An incident plane wave with amplitude $\phi_0 = 1$ traveling in $+X$ direction is given

$$\phi_I = \phi_0 e^{ikx}.$$

Case 1 In this case, the soft boundary conditions are considered. The number of coarse-mesh elements of the DL-FMBEM is set as 2700. Because there is no analytical solution for this example, the solution of the DL-FMBEM

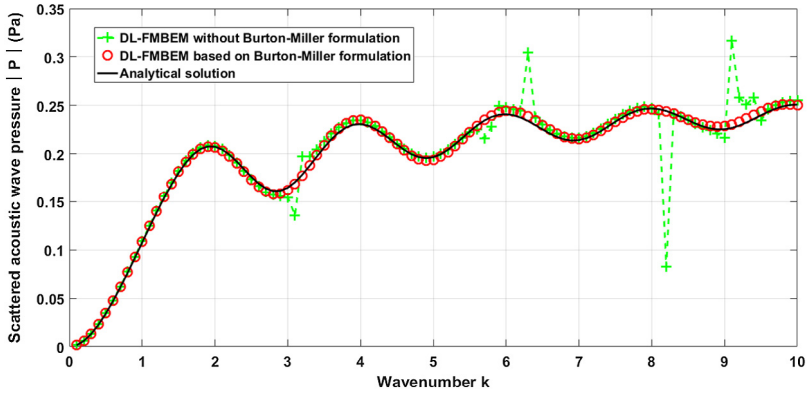

Fig. 10. Frequency-sweep plot of the scattered acoustic pressure $|P|$ (Pa) for the rigid sphere.

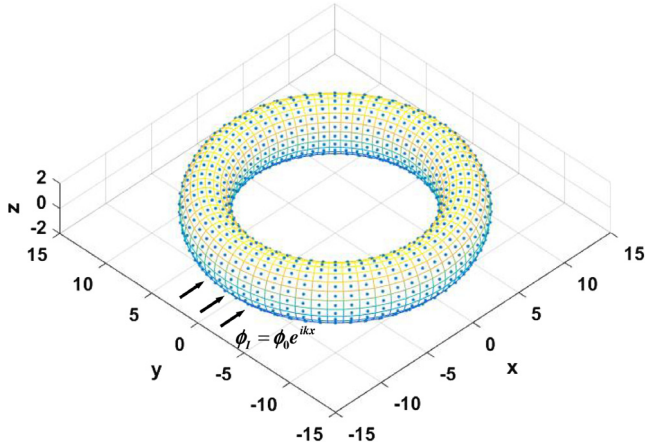

Fig. 11. The torus-shape obstacle.

based on the Burton–Miller formulation with 132 300 fine-mesh elements is used as a reference solution. The test points are placed on a sphere surface with radius 20 m. The convergent results of the DL-FMBEM based on the Burton–Miller formulation with 100 Hz, 200 Hz and 400 Hz are plotted respectively in Fig. 12.

It is observed from Fig. 12 that solutions of the DL-FMBEM based on the Burton–Miller formulation converge remarkably rapid with order of 3.5 for different test frequencies, where $k = 2\pi f/c$.

Case 2 The rigid boundary conditions are considered in this case. The number of coarse-mesh elements is taken as 4800, and number of fine-mesh elements is 43 200. The test frequency is set as $f = 400$ Hz. We plot the scattered sound pressure on the XZ plane as shown in Fig. 13a. Numerical results show that the consuming CPU time of the DL-FMBEM based on the Burton–Miller formulation is 575.82 s. The iteration number of *Step* 4–7 in the DL-FMBEM is 4, and $Rerr = 2.59\text{e}{-5}$.

For a comparison, we use COMSOL Multiphysics 5.3a to simulate the same problem. The computational domain is set as a cylinder with radius of 20 m and height of 6 m. We place 10 DOFs in each wavelength per direction, and the total number of DOFs is set as 4 836 663. The test frequency is also $f = 400$ Hz. Numerical report shows that the COMSOL uses 772 s to produce the similar results as given in Fig. 13b.

In Fig. 13a, we randomly take 50 points, and use solution of COMSOL as a reference solution. It is reported that the average relative error of solution of the DL-FMBEM based on the Burton–Miller formulation is 1.81%.

It should be mentioned that as a novel numerical methodology, the DL-FMBEM still has the space for further improvement, while as a mature commercial software, the code of the FEM in COMSOL has already been fully

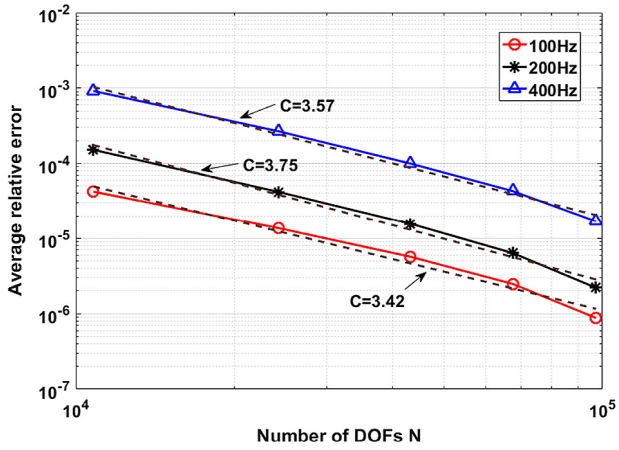

Fig. 12. Convergence of the DL-FMBEM based on the Burton–Miller formulation.

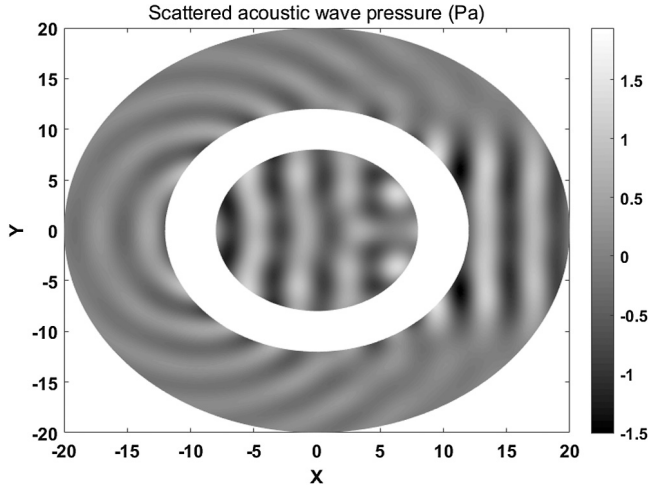

Fig. 13a. Scattered sound pressure evaluated by the DL-FMBEM based on the Burton–Miller formulation.

optimized. Even so, it is still observed that the CPU time and number of DOFs of the DL-FMBEM based on the Burton–Miller formulation are only about 75% and 0.89% of those of COMSOL, respectively.

Example 4. The underwater acoustic scattering characteristics of a Kilo-class submarine is investigated. Size of the submarine is 73.26 m×9.9 m×14.28 m as shown in Fig. 14. The sound speed c is set as 1480 m/s, i.e., the sound speed in water, and an incident plane wave with amplitude $\phi_0 = 1$ traveling in $-X$ direction is given

$$\phi_I = \phi_0 e^{-ikx}.$$

The sound pressure level is defined as

$$SPL = 20\log_{10}\left[p(e)/p(ref)\right], unit : \text{dB},$$

where the reference sound pressure $p\ (ref)$ is set as 1e−6 Pa.

Case 1 In this case, surface of the submarine is considered as a soft boundary condition. The number of coarse-mesh elements of the DL-FMBEM is set as 5207, and number of fine-mesh elements is 54 692. The test points are placed

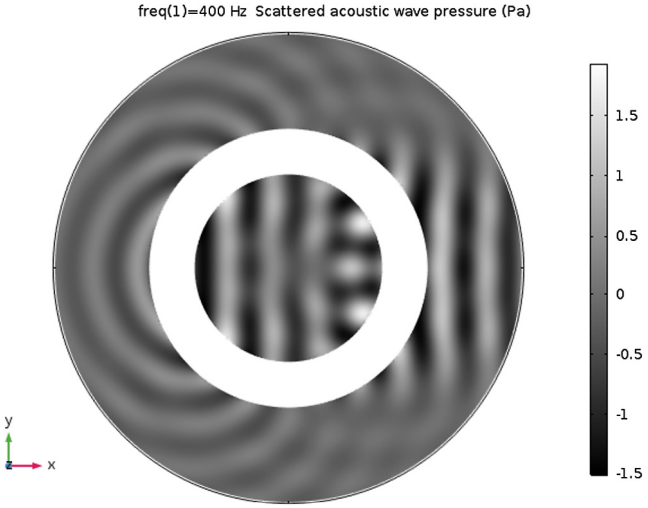

Fig. 13b. Scattered sound pressure evaluated by COMSOL.

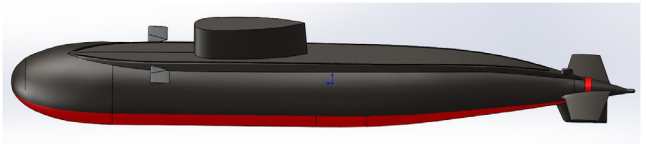

Fig. 14. The Kilo-class submarine model.

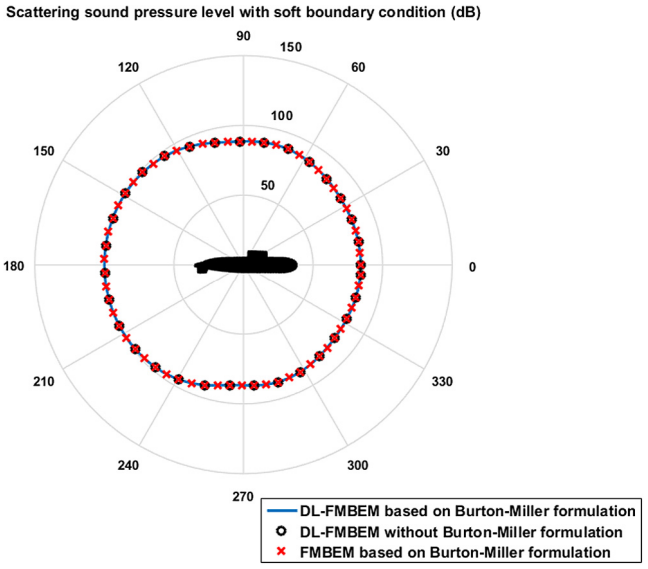

Fig. 15. Polar diagram of the acoustic scattering characteristics of the Kilo-class submarine.

on a circle with radius 200 m on the XY plane. We plot the polar diagram of the scattered sound pressure level with frequency $f = 20$ Hz as shown in Fig. 15. The $+X$ direction is set along 0° direction.

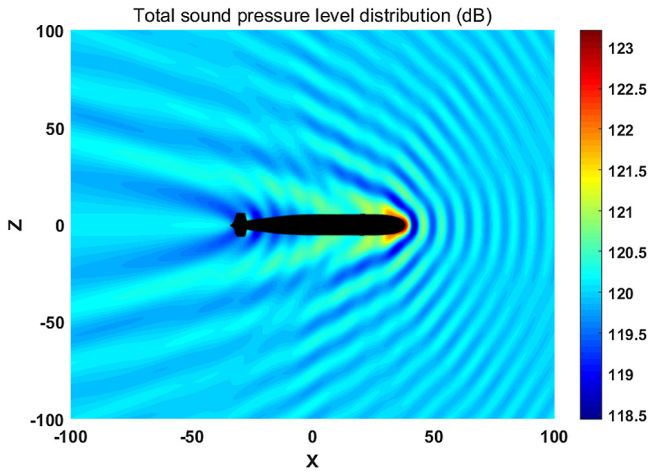

Fig. 16. Total sound pressure level distribution around the Kilo-class submarine.

If we use solution of the DL-FMBEM without the Burton–Miller formulation as a reference solution, the results show that errors of the DL-FMBEM based on the Burton–Miller formulation is $Error = 3.88\text{e}{-4}$ and $Rerr = 9.70\text{e}{-5}$. The CPU time is 297.17 s and the iterative number of *Step* 4–7 in the DL-FMBEM is 2.

To make a quick comparison, we use the FMBEM based on the Burton–Miller formulation with 54 692 DOFs to compute the same problem. Numerical results show that the FMBEM consumes 672.98 s to obtain the similar results with $Rerr = 9.84\text{e}{-5}$.

It should be mentioned that because the computational domain of this example is too large, COMSOL cannot analyze this problem under the similar computational conditions due to resources restriction of a single laptop.

Case 2 In this case, we consider the underwater acoustic scattering characteristics of the Kilo-class submarine with the rigid boundary conditions. The number of coarse-mesh elements of the DL-FMBEM is 5207, and number of fine-mesh elements is 102 396. We plot the total sound pressure level distribution with $f = 100$ Hz on the XZ plane as shown in Fig. 16.

Numerical results show that the DL-FMBEM consumes 1.08e+03 s to obtain the results with $Rerr = 7.44\text{e}{-5}$, and the iterative number of *Step* 4–7 in the DL-FMBEM is 7. It should be mentioned that because attenuation of the high frequency sound wave is very fast in water, the fast and efficient analysis of the large-scale low frequency sound field is very important for the research of underwater acoustic scattering characteristics of submarines.

Example 5. We analyze acoustic scattering characteristics of an A-320 aircraft having size of 39.03 m × 33.77 m × 4.33 m as shown in Fig. 17. The sound speed c is 343 m/s, and an incident plane wave with amplitude $\phi_0 = 1$ traveling in $-Z$ direction is given

$$\phi_I = \phi_0 e^{-ikz}.$$

The reference sound pressure p (*ref*) is defined as 2e−5 Pa.

Case 1 In this case, we consider acoustic scattering characteristics of the A-320 aircraft with the rigid boundary conditions. The number of coarse-mesh elements of the DL-FMBEM is set as 2689, and number of fine-mesh elements is 30 696. The test points are placed on a circle with radius 25 m on the XZ plane. We plot the polar diagram of the scattered sound pressure level with frequency $f = 20$ Hz as shown in Fig. 18. The $+X$ direction is set along 0° direction.

Numerical results show that error of the DL-FMBEM based on the Burton–Miller formulation is $Rerr = 5.99\text{e}{-5}$. The consuming CPU time is 1.43e+3 s, and the iterative number of *Step* 4–7 in the DL-FMBEM is 9. If solution of the DL-FMBEM without the Burton–Miller formulation is defined as a reference solution, it is observed that the average relative error of the DL-FMBEM based on the Burton–Miller formulation is $Error = 2.41\text{e}{-3}$.

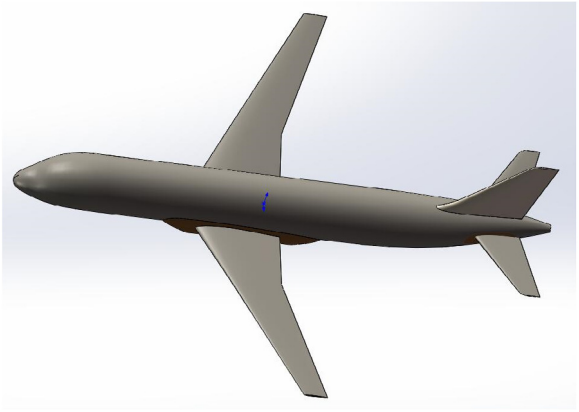

Fig. 17. An A-320 aircraft model.

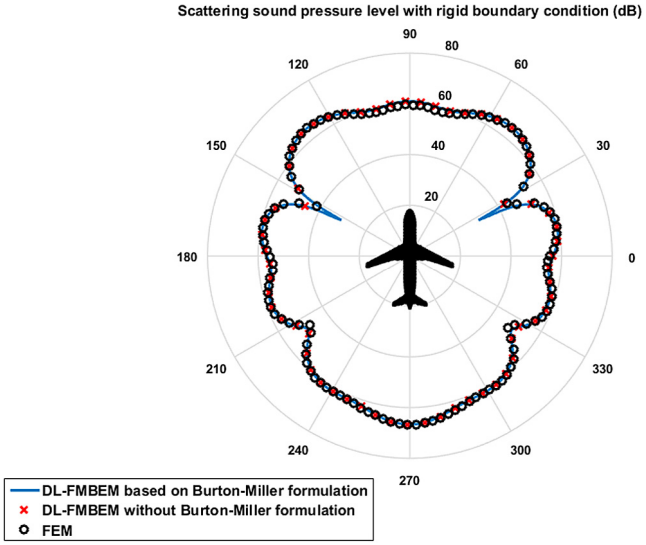

Fig. 18. Polar diagram of acoustic scattering characteristics of an A-320 aircraft.

Next, we use COMSOL to simulate the same problem. The computational domain is taken as a cylinder with radius of 25 m and height of 14 m. We place 30 DOFs in each wavelength per direction. The total number of DOFs is 4 562 979 and the test frequency is $f = 20$ Hz. Numerical results show that COMSOL uses 2554 s to obtain the similar results. If solution of the DL-FMBEM without the Burton–Miller formulation is employed as a reference solution, it is observed that the average relative error of the results of COMSOL is 1.37%.

It is noted that the CPU time and number of DOFs of the DL-FMBEM based on the Burton–Miller formulation are only about 55.82% and 0.67% of those of COMSOL, respectively. In comparison with the experimental data in Example 3, it is found that the relative CPU time of the DL-FMBEM significantly decreases. This is because that the dual-level structure has the preconditioning function to reduce the iteration number of GMRES solver. It is indicated that the DL-FMBEM is very efficient for analysis of the practical engineering problem, especially for such cases with complicated geometry domain and highly ill-conditioned interpolation matrix.

Case 2 In this case, we consider the scattering of sound wave with a soft boundary condition. The number of coarse-mesh elements of the DL-FMBEM is 20 340, and number of fine-mesh elements is 309 051. We plot the total sound pressure level distribution with $f = 100$ Hz on the XZ plane as shown in Fig. 19.

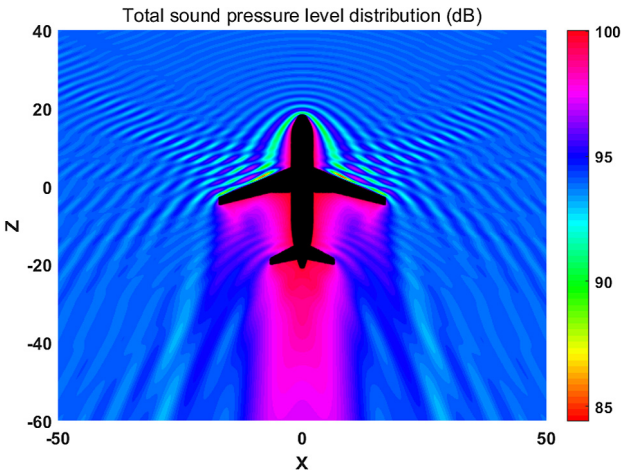

Fig. 19. Total sound pressure level distribution around the A-320 aircraft.

Numerical results show that the DL-FMBEM consumes 5.61e+3 s to obtain the solution with *Rerr* = 8.38e−5. The iterative number of *Step* 4–7 in the DL-FMBEM is 6. It should be mentioned that the dimensionless wavenumber reaches $kd = 71.5$ in this case, where d is the maximum diameter of the computational domain.

It is interesting to note that a similar problem was also investigated by using the diagonal form fast multipole singular boundary method (DF-FMSBM) [6,58]. In Ref. [6], the authors test sound scattering from a similar airplane having size of 33.2 m×25.5 m×7.1 m, where the number of boundary nodes is taken to be 125 822, the precision flag of the GMRES solver is set as 1e−3, the maximum number of boundary nodes allowed in a childless box is 100, and the test frequency f is 100 Hz ($kd = 60.8$). Numerical results show that the DF-FMSBM consumes 2644 s to obtain the acceptable results.

To make a quick comparison between the DL-FMBEM and the DF-FMSBM under the similar computational conditions, we set respectively the precision flag of the FMM, the DL-FMBEM and the GMRES solver as 5e−4, 1e−3 and 1e−3. The test frequency is set as 85 Hz ($kd = 60.8$). The number of coarse-mesh elements is taken as 5101, and number of fine-mesh elements is 127 789. Numerical results show that the DL-FMBEM consumes 515.41 s to obtain the similar solution with *Rerr* = 5.36e−4, and the iterative number of *Step* 4–7 in the DL-FMBEM is 3.

It is found that the CPU time of the DL-FMBEM is only 19.5% of that of the DF-FMSBM to obtain the similar results when one takes the same dimensionless wavenumber and similar number of DOFs.

4. Conclusions

In this study, a modified dual-level fast multipole boundary element method based on the Burton–Miller formulation is proposed for large-scale 3-D sound field analysis. Because of the application of the Burton–Miller formulation, it is observed that the non-uniqueness problem for exterior acoustic problems is solved. In addition, it is noted that the singular and hypersingular integrations are both avoided by using the subtraction and adding-back technique to solve the singularity and hypersingularity of the fundamental solutions at origin.

In comparison with the traditional FMBEM, it is observed that the DL-FMBEM is more efficient to solve the resulting large-scale linear system of equations having high condition number (L2-norm). For sound field analysis, it is also noted that the DL-FMBEM based on the Burton–Miller formulation achieves higher numerical efficiency and better performances than the traditional FEM as demonstrated in foregoing experiments.

Through simulating a variety of complicated engineering cases by using the DL-FMBEM based on the Burton–Miller formulation, the potential of the DL-FMBEM based on the Burton–Miller formulation for practical large-scale engineering analysis is verified to some extent. Numerical experiments show that the DL-FMBEM based on the Burton–Miller formulation performs about 56% faster than the traditional FMBEM in the analysis of underwater acoustic scattering characteristics of the Kilo-class submarine. In the analysis of acoustic scattering characteristics of an A-320 aircraft, the DL-FMBEM is about 44% faster than COMSOL.

5. Outlooks

Considering that the DL-FMBEM is much easier to program and use than the MLFMA, the DL-FMBEM appears computationally efficient and may be considered as a competitive alternative after further numerical and theoretical study. However, the present DL-FMBEM still has some issues to be further investigated:

1. Strict mathematical proof of the DL-FMBEM;
2. Combination of the DL-FMBEM with the high frequency FMM;
3. Development of a user-friendly software.

Acknowledgments

The work was supported by the Fundamental Research Funds for the Central Universities (Grant Nos. 2018B40714, 2017B709X14), the National Science Funds of China (Grant Nos. 11372097, 11572111), the Postgraduate Research & Practice Innovation Program of Jiangsu Province (Grant No. KYCX17_0488), the Postgraduate Scholarship Program from the China Scholarship Council (CSC) (Grant No. 201706710107).

Appendix. Derivation of the subtraction and adding-back technique

The subtraction and adding-back technique comes from the null-fields of boundary integral equation (BIE). The related code of the technique presented in this article is given in the Singularity Toolbox V2.0 at https://doi.org/10.13140/RG.2.2.13247.00162.

The null-fields of BIE of the Laplace equation is expressed as [59],

$$0 = \int_S \left[G_0(x, y) q(y) - \frac{\partial G_0(x, y)}{\partial n^e(y)} \phi(y) \right] dS(y), \forall x \in \Omega^e, \tag{A.1}$$

where the superscript e is the exterior domain, G_0 the fundamental solution of the 3-D Laplace equation,

$$\begin{cases} G_0(x, y) = \dfrac{1}{4\pi r} \\ \dfrac{\partial G_0(x, y)}{\partial n^e(y)} = -\dfrac{1}{4\pi r^2} \left\langle (x, y) \cdot n^e(y) \right\rangle. \end{cases} \tag{A.2}$$

The null-fields of HBIE of the Laplace equation is represented by

$$0 = \int_S \left[\frac{\partial G_0(x, y)}{\partial n^e(x)} q(y) - \frac{\partial^2 G_0(x, y)}{\partial n^e(y) \partial n^e(x)} \phi(y) \right] dS(y), \forall x \in \Omega^e, \tag{A.3}$$

where

$$\begin{cases} \dfrac{\partial G_0(x, y)}{\partial n^e(x)} = \dfrac{1}{4\pi r^2} \left\langle (x, y) \cdot n^e(x) \right\rangle \\ \dfrac{\partial^2 G_0(x, y)}{\partial n^e(y) \partial n^e(x)} = \dfrac{1}{4\pi r^3} \left[\left\langle n^e(x) \cdot n^e(y) \right\rangle - 3 \left\langle (x, y) \cdot n^e(x) \right\rangle \left\langle (x, y) \cdot n^e(y) \right\rangle \right]. \end{cases} \tag{A.4}$$

Substituting the general solution of the 3-D Laplace equation $\phi(y) = 1$ into Eqs. (A.1) and (A.3), Eqs. (A.1) and (A.3) are reformulated as

$$0 = \int_S \frac{\partial G_0(x, y)}{\partial n^e(y)} dS(y), \forall x \in \Omega^e, \tag{A.5}$$

$$0 = \int_S \frac{\partial^2 G_0(x, y)}{\partial n^e(y) \partial n^e(x)} dS(y), \forall x \in \Omega^e. \tag{A.6}$$

When a collocation point x approaches the boundary from the exterior domain, Eqs. (A.5) and (A.6) are discretized as

$$\sum_{j=1}^{N} \frac{\partial G_0(x_i, y_j)}{\partial n^e(y_j)} A_j = 0, \forall x_i \in S, \tag{A.7}$$

$$\sum_{i=1}^{N} \frac{\partial^2 G_0(x_i, y_j)}{\partial n^e(y_j)\partial n^e(x_i)} A_j = 0, \forall x_i \in S, \tag{A.8}$$

where A_j is the area of the jth element. Thus, we obtain the following formulations when $x_i = y_j$,

$$\frac{\partial G_0(x_i, y_i)}{\partial n^e(y_i)} = -\frac{1}{A_i} \sum_{j=1\neq i}^{N} \frac{\partial G_0(x_i, y_j)}{\partial n^e(y_j)} A_j, \forall x_i \in S, \tag{A.9}$$

$$\frac{\partial^2 G_0(x_i, y_i)}{\partial n^e(y_i)\partial n^e(x_i)} = -\frac{1}{A_i} \sum_{i=1\neq j}^{N} \frac{\partial^2 G_0(x_i, y_j)}{\partial n^e(y_j)\partial n^e(x_i)} A_j, \forall x_i \in S. \tag{A.10}$$

For a smooth boundary, assuming that the field point y_j approaches gradually the source point x_i along a line segment [60], we have

$$\lim_{y_j \to x_i} \frac{\partial G_0(x_i, y_j)}{\partial n^e(x_i)} + \frac{\partial G_0(x_i, y_j)}{\partial n^e(y_j)} = 0. \tag{A.11}$$

We hereby get

$$\frac{\partial G_0(x_i, y_i)}{\partial n^e(x_i)} = \frac{1}{A_i} \sum_{j=1\neq i}^{N} \frac{\partial G_0(x_i, y_j)}{\partial n^e(y_j)} A_j, \forall x_i \in S. \tag{A.12}$$

To derive the formulation of the $G_0(x_i, y_j)$ when $x_i = y_j$, the following general solution of the 3-D Laplace equation is introduced [43,61,62],

$$f(r) = \frac{1}{2} r^2, \tag{A.13}$$

$$\phi(y_j) = \frac{\partial f(y_j - x_i)}{\partial n^e(x_i)} = \left\langle (y_j - x_i) \cdot n^e(x_i) \right\rangle, \tag{A.14}$$

$$q(y_j) = \frac{\partial \phi(y_j)}{\partial n^e(y_j)} = \left\langle n^e(x_i) \cdot n^e(y_j) \right\rangle. \tag{A.15}$$

It is noted that the above general solution satisfies $\phi(y_i) = 0$ and $q(y_i) = 1$ when $x_i = y_j$. Substituting corresponding $\phi(y)$ and $q(y)$ into Eq. (A.1), we obtain Eq. (A.16) when the source point x approaches the boundary from exterior domain,

$$\sum_{j=1}^{N} \left[G_0(x_i, y_j) \left\langle n^e(x_i) \cdot n^e(y_j) \right\rangle - \frac{\partial G_0(x_i, y_j)}{\partial n^e(y_j)} \left\langle (y_j - x_i) \cdot n^e(x_i) \right\rangle \right] A_j = 0, \forall x_i \in S. \tag{A.16}$$

Then, we reformulate Eq. (A.16) in the following form,

$$G_0(x_i, y_i) = -\frac{1}{A_i} \sum_{j=1\neq i}^{N} \left[\begin{array}{l} G_0(x_i, y_j) \left\langle n^e(x_i) \cdot n^e(y_j) \right\rangle \\ -\dfrac{\partial G_0(x_i, y_j)}{\partial n^e(y_j)} \left\langle (y_j - x_i) \cdot n^e(x_i) \right\rangle \end{array} \right] A_j, \forall x_i \in S. \tag{A.17}$$

It is observed that the fundamental solutions of the 3-D Laplace equation and the 3-D Helmholtz equation have the same order of singularity at origin [63,64]. That is

$$\lim_{r\to 0} \frac{e^{ikr}}{4\pi r} = \lim_{r\to 0} \frac{\cos(kr)}{4\pi r} + \frac{\sin(kr)}{4\pi r} i = \lim_{r\to 0} \frac{1}{4\pi r} + \frac{k}{4\pi} i. \tag{A.18}$$

We have

$$G(x_i, y_i) = G_0(x_i, y_i) + \frac{k}{4\pi} i, r \to 0, \tag{A.19}$$

where $G = e^{ikr}/4\pi r$ is the fundamental solution of the 3-D Helmholtz equation.

Similarity, we obtain [63]

$$\frac{\partial G(x_i, y_i)}{\partial n^e(x_i)} = \frac{\partial G_0(x_i, y_i)}{\partial n^e(x_i)}, r \to 0, \tag{A.20}$$

$$\frac{\partial G(x_i, y_i)}{\partial n^e(y_i)} = \frac{\partial G_0(x_i, y_i)}{\partial n^e(y_i)}, r \to 0, \tag{A.21}$$

$$\frac{\partial^2 G(x_i, y_i)}{\partial n^e(y_i)\partial n^e(x_i)} = \frac{\partial^2 G_0(x_i, y_i)}{\partial n^e(y_i)\partial n^e(x_i)} + \frac{k^2}{2}\left[G_0(x_i, y_i) + \frac{k}{4\pi}i\right], r \to 0. \tag{A.22}$$

Making use of Eqs. (A.19)–(A.22), the singularities and hypersingularities in the BIE and HBIE [65,66] are avoided. It is noted that there are no integrations in these formulations.

References

[1] Y.G. Qu, J.P. Su, H.X. Hua, G. Meng, Structural vibration and acoustic radiation of coupled propeller-shafting and submarine hull system due to propeller forces, J. Sound Vib. 401 (2017) 76–93.

[2] X.M. Wang, S. Liu, Z.P. Liu, Underwater sonar image detection: A combination of non-local spatial information and quantum-inspired shuffled frog leaping algorithm, PLoS One 12 (2017) 1–30.

[3] A. Brancati, M.H. Aliabadi, V. Mallardo, A BEM sensitivity formulation for three-dimensional active noise control, Internat. J. Numer. Methods Engrg. 90 (2012) 1183–1206.

[4] J.P. Li, W. Chen, A modified singular boundary method for three-dimensional high frequency acoustic wave problems, Appl. Math. Model. 54 (2018) 189–201.

[5] E. Giladi, Asymptotically derived boundary elements for the Helmholtz equation in high frequencies, J. Comput. Appl. Math. 198 (2007) 52–74.

[6] W.Z. Qu, W. Chen, C.J. Zheng, Diagonal form fast multipole singular boundary method applied to the solution of high-frequency acoustic radiation and scattering, Internat. J. Numer. Methods Engrg. 111 (2017) 803–815.

[7] S. Kim, C.S. Shin, J.B. Keller, High-frequency asymptotics for the numerical solution of the Helmholtz equation, Appl. Math. Lett. 18 (2005) 797–804.

[8] O.G. Ernst, M.J. Gander, Why it is difficult to solve Helmholtz problems with classical iterative methods, in: I.G. Graham, T.Y. Hou, O. Lakkis, R. Scheichl (Eds.), Numerical Analysis of Multiscale Problems, Springer, Berlin, 2012, pp. 325–363.

[9] Y.A. Erlangga, Advances in iterative methods and preconditioners for the Helmholtz equation, Arch. Comput. Methods Eng. 15 (2008) 37–66.

[10] Q.H. Qin, H. Wang, Matlab and C Programming for Trefftz Finite Element Methods, CRC press, Boca Raton, 2009.

[11] F. Magoulès, H.Y. Zhang, Three-dimensional dispersion analysis and stabilised finite element methods for acoustics, Comput. Methods Appl. Mech. Engrg. 335 (2018) 563–583.

[12] Y.B. Chai, Z.X. Gong, W. Li, T.Y. Li, Q.F. Zhang, A smoothed finite element method for exterior Helmholtz equation in two dimensions, Eng. Anal. Bound. Elem. 84 (2017) 237–252.

[13] Q.H. Qin, Hybrid Trefftz finite-element approach for plate-bending on an elastic-foundation, Appl. Math. Model. 18 (1994) 334–339.

[14] I.M. Babuska, S.A. Sauter, Is the pollution effect of the FEM avoidable for the Helmholtz equation considering high wave numbers? SIAM Rev. 42 (2000) 451–484.

[15] Y. Gu, X.Q. He, W. Chen, C.Z. Zhang, Analysis of three-dimensional anisotropic heat conduction problems on thin domains using an advanced boundary element method, Comput. Math. Appl. 75 (2018) 33–44.

[16] Q.H. Qin, Green's Function and Boundary Elements of Multifield Materials, Elsevier, Oxford, 2007.

[17] R. Ohayon, C. Soize, Vibration of structures containing compressible liquids with surface tension and sloshing effects reduced-order model, Comput. Mech. 55 (2015) 1071–1078.

[18] Q.H. Qin, Nonlinear-analysis of Reissner plates on an elastic-foundation by the BEM, Int. J. Solids Struct. 30 (1993) 3101–3111.

[19] H.G. Sun, X.T. Liu, Y. Zhang, G.F. Pang, R. Garrard, A fast semi-discrete Kansa method to solve the two-dimensional spatiotemporal fractional diffusion equation, J. Comput. Phys. 345 (2017) 74–90.

[20] Z.J. Fu, W. Chen, P.H. Wen, C.Z. Zhang, Singular boundary method for wave propagation analysis in periodic structures, J. Sound Vib. 425 (2018) 170–188.

[21] A. Brancati, M.H. Aliabadi, A. Milazzo, An improved hierarchical ACA technique for sound absorbent materials, Comput. Model. Eng. Sci. 78 (2011) 1–24.

[22] J.P. Li, Z.J. Fu, W. Chen, Numerical investigation on the obliquely incident water wave passing through the submerged breakwater by singular boundary method, Comput. Math. Appl. 71 (2016) 381–390.

[23] J.P. Li, W. Chen, Y. Gu, Error bounds of singular boundary method for potential problems, Numer. Methods Partial Differential Equations 33 (2017) 1987–2004.

[24] J. Lin, C.Z. Zhang, L.L. Sun, J. Lu, Simulation of seismic wave scattering by embedded cavities in an elastic Half-Plane using the novel singular boundary method, Adv. Appl. Math. Mech. 10 (2018) 322–342.

[25] F.J. Wang, W. Chen, A. Tadeu, C.G. Correia, Singular boundary method for transient convection–diffusion problems with time-dependent fundamental solution, Int. J. Heat Mass Transfer 114 (2017) 1126–1134.

[26] Q.G. Liu, B. Šarler, A non-singular method of fundamental solutions for two-dimensional steady-state isotropic thermoelasticity problems, Eng. Anal. Bound. Elem. 75 (2017) 89–102.

[27] H. Wang, Q.H. Qin, A meshless method for generalized linear or nonlinear Poisson-type problems, Eng. Anal. Bound. Elem. 30 (2006) 515–521.

[28] Y. Sun, S.N. He, A meshless method based on the method of fundamental solution for three-dimensional inverse heat conduction problems, Int. J. Heat Mass Transfer 108 (2017) 945–960.

[29] H. Wang, Q.H. Qin, Meshless approach for thermo-mechanical analysis of functionally graded materials, Eng. Anal. Bound. Elem. 32 (2008) 704–712.
[30] J.F. Huang, J. Jia, B. Zhang, FMM-Yukawa: An adaptive fast multipole method for screened Coulomb interactions, Comput. Phys. Comm. 180 (2009) 2331–2338.
[31] Y.J. Liu, S. Mukherjee, N. Nishimura, W. Ye, A. Sutradhar, E. Pan, N.A. Dumont, A. Frangi, A. Saez, Recent advances and emerging applications of the boundary element method, Appl. Mech. Rev. 64 (2011) 1001–1037.
[32] L. Greengard, The Rapid Evaluation of Potential Fields in Particle Systems, MIT Press, Cambridge, 1988.
[33] W.W. Li, W. Chen, Z.F. Fu, Precorrected-FFT accelerated singular boundary method for large-scale three-dimensional potential problems, Commun. Comput. Phys. 22 (2017) 460–472.
[34] C.C. Weng, T.J. Cui, J.M. Song, A FAFFA-MLFMA algorithm for electromagnetic scattering, IEEE Trans. Antennas and Propagation 50 (2002) 1641–1649.
[35] T.J. Cui, C.C. Weng, G. Chen, J. Song, Efficient MLFMA, RPFMA, and FAFFA algorithms for EM scattering by very large structures, IEEE Trans. Antennas and Propagation 52 (2004) 759–770.
[36] E.J. Kansa, P. Holoborodko, On the ill-conditioned nature of C ∞ RBF strong collocation, Eng. Anal. Bound. Elem. 78 (2017) 26–30.
[37] P.C. Hansen, Regularization tools version 4.0 for Matlab 7.3., Numer. Algorithms 46 (2007) 189–194.
[38] Y. Saad, M.H. Schultz, GMRES: A generalized minimal residual algorithm for solving nonsymmetric linear systems, SIAM J. Sci. Stat. Comput. 7 (1986) 856–869.
[39] L. Greengard, J.F. Huang, V. Rokhlin, S. Wandzura, Accelerating fast multipole methods for the Helmholtz equation at low frequencies, IEEE Comput. Sci. Eng. 5 (1998) 32–38.
[40] H.J. Wu, Y.J. Liu, W.K. Jiang, A low-frequency fast multipole boundary element method based on analytical integration of the hypersingular integral for 3D acoustic problems, Eng. Anal. Bound. Elem. 37 (2013) 309–318.
[41] V. Rokhlin, Diagonal forms of translation operators for the Helmholtz equation in three dimensions, Appl. Comput. Harmon. Anal. 1 (1993) 82–93.
[42] H.J. Wu, Y.J. Liu, W.K. Jiang, Analytical integration of the moments in the diagonal form fast multipole boundary element method for 3-D acoustic wave problems, Eng. Anal. Bound. Elem. 36 (2012) 248–254.
[43] J.P. Li, W. Chen, Z.J. Fu, A modified dual-level algorithm for large-scale three-dimensional Laplace and Helmholtz equation, Comput. Mech. (2018). http://dx.doi.org/10.1007/s00466-018-1536-2.
[44] A.J. Burton, G.F. Miller, The application of integral equation methods to the numerical solution of some exterior boundary-value problems, Proc. R. Soc. Lond. Ser. A 323 (1971) 201–210.
[45] Q.H. Qin, The Trefftz Finite and Boundary Element Method, WIT Press, Southampton, 2000.
[46] C.A. Brebbia, Progress in Boundary Element Methods, second ed., Springer-Verlag, New York, 1981.
[47] J. Dölz, H. Harbrecht, S. Kurz, S. Schöps, F. Wolf, A fast isogeometric BEM for the three dimensional laplace- and helmholtz problems, Comput. Methods Appl. Mech. Engrg. 330 (2018) 83–101.
[48] S. Keuchel, N.C. Hagelstein, O. Zaleski, O. Vonestorff, Evaluation of hypersingular and nearly singular integrals in the Isogeometric Boundary Element Method for acoustics, Comput. Methods Appl. Mech. Engrg. 325 (2017) 488–504.
[49] S. Marburg, T.W. Wu, Treating the phenomenon of irregular frequencies, in: S. Marburg, B. Nolte (Eds.), Computational Acoustics of Noise Propagation in Fluids, Springer, Berlin, 2008, pp. 411–434.
[50] J.P. Li, W. Chen, Singular boundary method based on time-dependent fundamental solutions for active noise control, Numer. Methods Partial Differential Equations 34 (2018) 1401–1421.
[51] J.P. Li, W. Chen, Z.J. Fu, L.L. Sun, Explicit empirical formula evaluating original intensity factors of singular boundary method for potential and Helmholtz problems, Eng. Anal. Bound. Elem. 73 (2016) 161–169.
[52] L.L. Sun, W. Chen, A.H.D. Cheng, Evaluating the origin intensity factor in the singular boundary method for three-dimensional Dirichlet problems, Adv. Appl. Math. Mech. 9 (2017) 1289–1311.
[53] L. Shen, Y.J. Liu, An adaptive fast multipole boundary element method for three-dimensional acoustic wave problems based on the Burton-Miller formulation, Comput. Mech. 40 (2007) 461–472.
[54] Y.J. Liu, Fast Multipole Boundary Element Method: Theory and Applications in Engineering, Cambridge University Press, Cambridge, 2009.
[55] L. Shen, Y.J. Liu, An adaptive fast multipole boundary element method for three-dimensional potential problems, Comput. Mech. 39 (2007) 681–691.
[56] N. Nishimura, Fast multipole accelerated boundary integral equation methods, Appl. Mech. Rev. 55 (2002) 299–324.
[57] J.T. Chen, Y.T. Lee, Y.J. Lin, Analysis of mutiple-shepers radiation and scattering problems by using a null-field integral equation approach, Appl. Acoust. 71 (2010) 690–700.
[58] W.Z. Qu, W. Chen, Y. Gu, Fast multipole accelerated singular boundary method for the 3D Helmholtz equation in low frequency regime, Comput. Math. Appl. 70 (2015) 679–690.
[59] J. Jirousek, Q.H. Qin, Application of hybrid-Trefftz element approach to transient heat-conduction analysis, Comput. Struct. 58 (1996) 195–201.
[60] D.L. Young, K.H. Chen, C.W. Lee, Novel meshless method for solving the potential problems with arbitrary domain, J. Comput. Phys. 209 (2005) 290–321.
[61] L. Liu, H. Zhang, Single layer regularized meshless method for three dimensional Laplace problem, Eng. Anal. Bound. Elem. 71 (2016) 164–168.
[62] L. Liu, Single layer regularized meshless method for three dimensional exterior acoustic problem, Eng. Anal. Bound. Elem. 77 (2017) 138–144.

[63] Z.J. Fu, W. Chen, Y. Gu, Burton-Miller-type singular boundary method for acoustic radiation and scattering, J. Sound Vib. 333 (2014) 3776–3793.
[64] W. Chen, J.P. Li, Z.J. Fu, Singular boundary method using time-dependent fundamental solution for scalar wave equations, Comput. Mech. 58 (2016) 717–730.
[65] D.L. Young, K.H. Chen, T.Y. Liu, L.H. Shen, C.S. Wu, Hypersingular meshless method for solving 3D potential problems with arbitrary domain, Comput. Model. Eng. Sci. 40 (2009) 225–269.
[66] H.J. Wu, W.J. Ye, W.K. Jiang, A collocation BEM for 3D acoustic problems based on a non-singular Burton–Miller formulation with linear continuous elements, Comput. Methods Appl. Mech. Engrg. 332 (2018) 191–216.